CANCER

Concurrence of extracellular vesicle enrichment and metabolic switch visualized label-free in the tumor microenvironment

Haohua Tu,[1]*† Yuan Liu,[1,2]* Marina Marjanovic,[1,2] Eric J. Chaney,[1] Sixian You,[1,2] Youbo Zhao,[1] Stephen A. Boppart[1,2,3,4]†

Understanding the role of the tumor microenvironment in carcinogenesis has reshaped cancer research. Events at both microscopic (molecular) and macroscopic (tissue) scales have been identified in engineered tumor microenvironments involving in vitro cultures, live tissue xenografts, and transgenic animals. However, these events have not been comprehensively observed under unperturbed (authentic) conditions free of exogenous labeling or genetic modification. The lack of a suitable imaging methodology has largely limited our understanding of the complex interrelations and possible causal links involved in carcinogenesis and metastasis within the tumor microenvironment. Using multicontrast nonlinear imaging, we visualize endogenous substances in rat and human mammary tumors through their intrinsic nonlinear optical properties, and simultaneously observe angiogenesis, extracellular matrix reorganization, and non-native cell recruitment. We find that all these macroscopic events in the tumor microenvironment require concurrent enrichment of specific extracellular vesicles and a metabolic switch toward biosynthesis. This concurrence at the microscopic scale provides not only new insights into carcinogenesis and metastasis but also a potentially new strategy for cancer diagnosis, surgery, and therapeutics.

INTRODUCTION

The tumor microenvironment has been represented by a nonreductionist view of cancer (1), interactions at the tumor-host interface (2), a wound-healing analog of tumor development (3), the concept of "seed and soil" (4), the bipolar effects of stroma in the tumor "organ" (5), and the Darwinian (environmental) selection of metastatic tumor cells (4, 6). Signature events occurring in the tumor microenvironment include (i) recruitment or infiltration of non-native cells, such as immune inflammatory cells (7) and bone marrow–derived cells (8), and activation or alteration of fibroblasts (9) or other native cells for promotion of tumor malignancy and protection from immune attack; (ii) a mechanically reorganized extracellular matrix, including degraded basement membrane (10) and rearranged, cross-linked, or fibrotic collagen (11) for enhanced local invasion (12); (iii) angiogenesis (13, 14) and lymphangiogenesis (15) for primary tumor growth and subsequent metastasis; (iv) modulation of stroma by small (<1 μm) tumor-associated extracellular vesicles for preconditioning proliferation, invasion, and metastasis of tumor cells (16); and (v) a metabolic switch from energy production to biomass production (biosynthesis), that is, a reinterpreted Warburg effect that enriches amino acids, nucleotides, and fatty acids (17). The metabolic switch has long been masked in oxygen- and nutrient-rich tissue cultures and has therefore been treated as an adaption to the stressful tumor microenvironment (18). Each of these tumor microenvironment events has been investigated with exogenous molecular labeling probes to identify biomolecules of interest (rare signaling molecules or bulk substances) within biological samples (cell/tissue cultures, xenografts, dissected specimens, transgenic animals, cancer animal models, living subjects, etc.) under in vitro, ex vivo, intravital, or in vivo conditions (19, 20). However, the interrelation between the events at the macroscopic scale (i to iii) and microscopic scale (iv and v) remains elusive because of the lack of an imaging methodology to observe them in concert, in spatially resolved ways, and without perturbative labels.

Optical imaging can be a promising approach (21) to study this interrelation if molecular labeling agents, including genetic reporters that may affect the living system through genetic manipulation, are avoided to eliminate unexpected perturbations to the tumor microenvironment. In addition, to retain more authentic physiology during carcinogenesis, imaging should be performed in nonxenograft tissues and using a reflection mode (epi-)geometry so that these events can be potentially monitored in future clinical scenarios to evaluate therapeutic strategies (1–19). Along this path, linear microscopy techniques using photoacoustics (22) or optical frequency domain imaging (23) targeting single-photon absorption or scattering contrast have visualized angiogenesis and lymphangiogenesis. However, the desired high spatial resolution, free of exogenous labeling, is gained at the price of molecular specificity, which is crucial in the era of molecular oncology (19, 20). Alternatively, nonlinear microscopy targeting two-photon optical noncentrosymmetry contrast $\chi^{(2)}_{SHG}$ (24, 25) and three-photon excited autofluorescence contrast $AF^{(3)}$ (26, 27) has imaged reorganized collagen and intrinsic fluorophores, respectively. Similarly, nonlinear microscopy has further visualized tumor cells through two-photon excited autofluorescence contrast $AF^{(2)}$ (28) and blood cells/vessels through the molecular vibration contrast of coherent anti-Stokes Raman scattering (CARS) $\chi^{(3)}_{CARS}$ (29). Thus, previously used cell-tracking fluorescent proteins (25) and injected angiogenesis-revealing agents (30) may be avoided. In addition, the $\chi^{(3)}_{CARS}$ contrast and three-photon optical heterogeneity contrast $\chi^{(3)}_{THG}$ have revealed the metabolic alteration to lipid/protein ratio (31, 32) and the release of extracellular vesicles in tissue (33), respectively.

[1]Beckman Institute for Advanced Science and Technology, University of Illinois at Urbana-Champaign, Urbana, IL 61801, USA. [2]Department of Bioengineering, University of Illinois at Urbana-Champaign, Urbana, IL 61801, USA. [3]Department of Electrical and Computer Engineering, University of Illinois at Urbana-Champaign, Urbana, IL 61801, USA. [4]Department of Medicine, University of Illinois at Urbana-Champaign, Urbana, IL 61801, USA.
*These authors contributed equally to this work.
†Corresponding author. Email: htu@illinois.edu (H.T.); boppart@illinois.edu (S.A.B.)

By demonstrating the versatility of nonlinear microscopy, these scattered efforts encouraged us to develop a multicontrast (multimodal) nonlinear imaging platform (34) capable of collecting spatially coregistered images with different contrasts (figs. S1 and S2 and table S1). We recovered the molecular specificity and were able to simultaneously observe all tumor microenvironment events (i to v) in a well-established preclinical carcinogen-induced (nontransgenic) rat mammary tumor model (35). We seek to visualize the interrelations and spatial relationships among these events and document the unusual concurrence of extracellular vesicle enrichment and a metabolic switch that underlies important steps in early cancer development.

RESULTS

Multicontrast imaging of unperturbed tumor microenvironments

Mammary tumor microenvironments in a carcinogen-induced rat model were investigated by multicontrast nonlinear imaging in a 9-week longitudinal study (see Table 1 and Materials and Methods). For example, in week 7 of tumor development, largely different and orthogonalized contrasts can be obtained from the same focal plane of an ex vivo mammary tumor (Fig. 1 and fig. S2). In particular, each pair of contrasts from harmonic generation (Fig. 1A), autofluorescence (Fig. 1B), and molecular vibration (fig. S2, A and B; Raman response at xxxx cm^{-1} is abbreviated as Rxxxx hereafter) is orthogonal to each other, reflecting local optical structure, redox activity (28), and lipid-protein transition (31, 32), respectively. The substances selectively revealed (or "artificially labeled") by one contrast (fig. S2, A to F), when placed against the "background" of the other contrasts (fig. S2, A to L), allow unambiguous recognition of various macroscopic structures or events (Fig. 1) and new functional knowledge that is largely absent in lower dimensional multicontrast images (table S2), just as with conventional fluorescence-labeled imaging.

The light excitation/detection switched among $\chi^{(2)}_{SHG}$, $\chi^{(3)}_{THG}$, $AF^{(2)}$, $AF^{(3)}$, $\chi^{(3)}_{R2850}$, and $\chi^{(3)}_{R3050}$ plays an analogous role to six exogenous fluorescent dyes but with no known perturbation to the structure, molecular composition, or function of the biological sample. This results in the marked emergence of many micrometer-sized $AF^{(3)}$-visible vesicles from $AF^{(2)}$-visible vascular features during the transition from the $AF^{(2)}$ image to the $AF^{(3)}$ image (Fig. 1B and fig. S2E). Other classes of micrometer-sized vesicles (table S3), including lipid vesicles and $\chi^{(3)}_{THG}$-$AF^{(3)}$–covisible vesicles, are observed to be coregistered in images based on multiple different contrasts (fig. S2, A to F). This cross-contrast visibility provides independent confirmation and classification of spatially disorganized vesicles without sample motion artifacts, allows automatic identification of their locations and distributions by straightforward image processing, and validates the coregistered multicontrast imaging at the same imaging plane. Our ability to observe a wide variety of endogenous vesicles in the tumor microenvironments will facilitate future studies on their physiochemical properties and biological functions.

In addition to palpable tumors at a late stage (weeks 3 to 9) of tumor development, four additional types of samples were also imaged (Table 1): (i) "control" mammary specimens from rats without carcinogen injection, (ii) "normal" samples defined as the normal-appearing mammary tissue in early-stage (weeks 1 and 2) tumor development, free of palpable tumors or 10 mm away from palpable tumors in late-stage tumor development, (iii) "temporally precancerous" samples free of palpable tumors but suspicious of early-stage cancer development by visual (gross) inspection, and (iv) "spatially precancerous"

samples resected 2 to 5 mm away from palpable tumors suspicious of precancerous development by visual inspection. The typical field of view of nontumor (control or normal) samples consists of approximately 80% adipocyte-dominated regions (Fig. 2, main) with 20% stromal regions (Fig. 2, insets 1 and 2). The extensive image analysis of tumor and nontumor samples enables the differentiation of observed macroscopic tumor microenvironment events (7–15) from certain nontumor macroscopic events (table S4), as discussed below.

Extracellular vesicle enrichment in stroma

The $\chi^{(3)}_{THG}$-$AF^{(3)}$–covisible vesicles are obscured by a strong $AF^{(2)}$ background in Fig. 1 but revealed in the $\chi^{(3)}_{THG}$ image of fig. S2F. These vesicles reside in certain $AF^{(2)}$-visible cells (colocalized red arrows in Fig. 1, A and B) and are released into various stromal regions with thin elastin fibers, dense collagen, angiogenesis, and lipid breakdown (fig. S2F). Moreover, except for two samples from a necrotic tumor and another sample from an abnormal control rat (7_control/b in Table 1A), these vesicles are systematically more abundant in tumors than in nontumor samples, with little dependence on sample spatial heterogeneity (Table 1A). Thus, we attribute the $\chi^{(3)}_{THG}$-$AF^{(3)}$–covisible vesicles to tumor-associated extracellular vesicles likely originating from the tumor cells at the tumor boundary (Fig. 1, A and B). The otherwise normal adipocytes [with $AF^{(2)}$-visible cytoplasm located at interstitial spaces among large lipids] and stromal cells free of these vesicles (pink arrows in Fig. 2) seem to transform by accepting and concentrating the vesicles (Fig. 1, A and B; malignant adipocytes or stromal cells). It appears that the stroma is modulated by these vesicles during carcinogenesis (16).

These extracellular vesicles cannot be discriminated against the "benign" $\chi^{(3)}_{R2850}$-$\chi^{(3)}_{THG}$–covisible lipid vesicles (29, 36) by $\chi^{(3)}_{THG}$ contrast alone but disappear from the $\chi^{(3)}_{THG}$ image when the contrast is instantly switched to $\chi^{(3)}_{R2850}$ (compare fig. S2F with fig. S2B). This discrimination strategy, termed as "tracking disappearances in a different light" (as opposed to "seeing things in a different light" exhibited by fig. S2, A to F), sets our assignment apart from the previous study that assigned all $\chi^{(3)}_{THG}$-visible vesicles as tumor-associated extracellular vesicles (33). The interfering lipid vesicles can migrate to the extracellular stromal regions of collagen fibers (Fig. 2, inset 1; termed as "stromal lipid dispersion" in table S4) but exhibit no disparate prevalence in tumor and nontumor samples. They would thus mask the key statistical evidence that identifies the tumor-associated extracellular vesicles (Table 1A).

(Lymph-)angiogenesis and extracellular matrix reorganization

The observed $AF^{(3)}$-visible vesicles appear related to the blood vessels during angiogenesis. Using their density to estimate the stages of angiogenesis (Fig. 1), we can classify the observed vessels or capillaries as (i) developed vessels with less or no vesicles but a $\chi^{(3)}_{R2850}$-$AF^{(2)}$–covisible vessel wall, (ii) developing vessels with more vesicles and a high internal $AF^{(2)}$ signal but no detectable vessel wall, and (iii) emerging vessels with abundant vesicles but neither a high internal $AF^{(2)}$ signal nor a well-defined vessel wall. The hyperspectral imaging of $\chi^{(3)}_{CARS}$ (see Materials and Methods) confirms a developing blood vessel by revealing its internal flow (movie S1). Another category of vessels with larger diameters and poorly organized (leaky) $AF^{(2)}$-visible walls may be attributed to lymphatic vessels because they do not have the continuous $\chi^{(3)}_{R2850}$-visible vessel wall characteristic of the developed blood vessels (29). These lymphatic vessels can be similarly classified as developing

Tu et al. Sci. Adv. 2017;3:e1600675   25 January 2017

2 of 13

Table 1. Longitudinal animal test of extracellular vesicles and $\chi^{(3)}_{R3050}$ as quantitative breast cancer indicators within (A) a constant field of view (0.19 × 0.19 mm²) and (B) a larger field of view (0.57 × 0.57 mm²). Nontumor (control or normal), tumor, spatially precancerous (resected 2 to 5 mm away from a palpable tumor), temporally precancerous (with no palpable tumor), and two samples from an abnormal control rat are highlighted in green, red, violet, orange, and blue, respectively, in the first column. The tumor (on site), spatially precancerous, and normal-appearing samples (resected 10 mm away from a palpable tumor) linked by one palpable tumor are shaded together in the second column. For the diagnosis by visual inspection, "−" represents white and thin mammary gland, "+" represents palpable tumor mass with orange color and rice-like granular formation, and "+/−" represents slightly darker mammary gland suspicious of tumor development. Tumor-associated extracellular vesicles are automatically recognized from $\chi^{(3)}_{THG}$ images by a software procedure that quantifies the prominence of a candidate vesicle and its FWHM size. For the diagnosis by vesicle count, "+" represents more than six counts, and "−" represents less than six counts. Samples with inconsistent diagnosis from visual inspection and two quantitative cancer indicators (vesicle count and the presence of R3050 peak) are highlighted in red in the third, fourth, and fifth columns. For the classification of a sampling (imaging) site, "A" represents adipocyte region, "S" represents stromal region, and "T" represents tumor region. All images collected in the longitudinal animal study are included for unbiased statistical analysis.

A

Week_rat/ sampling site	Site related to tumor	Visual	Vesicles, count	R3050	Class	Tumor microenvironment events* and other biological structures/events (figure reference)
1_control/a		−	−, 1	−	A&S	Lipid breakdown
1_control/b		−	−, 0	−	A&S	Lipid breakdown
1_control/c		−	−, 1	−	S	Collagen production, lipolysis
1_experiment/a		−	−, 0	−	A&S	Lipogenesis, lipid breakdown, stromal native cells
1_experiment/b		+/−	+, >20	+	S	Hair follicle
1_experiment/c		+/−	+, 9	+	S	Mammary duct, lipolysis
1_experiment/d		−	−, 0	−	A&S	Nerve, stromal native cells
2_control/a		−	−, 0	−	A	Fluorescent protein mass
2_control/b		−	−, 0	−	S	Native cells, lipolysis
2_control/c		−	−, 0	−	A	Regular adipocytes
2_experiment/a		−	−, 1	−	S	Native cells, mammary duct
2_experiment/b		−	−, 2	−	S	Mammary duct, lipolysis, native cells (Fig. 2, inset 2)
2_experiment/c		−	−, 5	−	S	Stromal native cells
2_experiment/d		−	−, 4	−	A&S	Nerve
2_experiment/e		−	−, 0	−	A&S	Nerve
3_control/a		−	−, 2	−	A	Lipolysis
3_control/b		−	−, 0	−	A	Regular adipocytes
3_control/c		−	−, 4	−	S	Collagen production, native cells, nerve
3_experiment/a		+	+, >20	+	A&S	**Lymphangiogenesis**, stromal native cells, fluorescent protein mass
3_experiment/b		+	+, >20	+	T&S	**Collagen cross-linking**, tumor (cells)
3_experiment/c		−	−, 1	−	A	Regular adipocytes
3_experiment/d		−	−, 0	−	A&S	Stromal native cells
3_experiment/e		−	−, 4	−	A&S	Collagen ring
4_control/a		−	−, 0	−	A	Regular adipocytes, native cells among adipocytes, crystallization
4_control/b		−	−, 0	−	A&S	Lipid breakdown, native cells
4_experiment/a	On site	+	+, >20	+	A&S	Lipid breakdown
4_experiment/b	On site	+	+, 10	+	A&S	**Fibrosis**, stromal native cells

continued on next page

A

Week_rat/ sampling site	Site related to tumor	Visual	Vesicles, count	R3050	Class	Tumor microenvironment events* and other biological structures/events (figure reference)
4_experiment/c	On site	+	+, >20	+	T	**Collagen cross-linking**, tumor (cells)
4_experiment/d	2–5 mm	+/−	+, 13	+	A&S	Lipid breakdown, crystallization
5_control/a		−	−, 0	−	S	Lipolysis
5_control/b		−	−, 3	−	A&S	Lipolysis
5_control/c		−	−, 0	−	S	Stromal lipid dispersion, lipolysis
5_experiment/a	On site	+	+, 8	+	T/S	**Basement membrane degradation, reorganized collagen**, tumor (cells)
5_experiment/b	On site	+	+, 18	+	A&S	**Non-native cell recruitment**, collagen production, stromal native cells (Fig. 3E)
5_experiment/c	On site	+	+, 17	+	T	**Basement membrane degradation, non-native cell recruitment, reorganized collagen**, tumor (cells) (Fig. 3C)
5_experiment/d	On site	+	+, >20	+	S&T	**Angiogenesis**, blood cells, tumor (cells)
5_experiment/e	On site	+	+, 9	+	A&S	Lipid breakdown
5_experiment/f	10 mm	−	−, 0	−	A&S	Lymphatic vessel, stromal native cells
5_experiment/g	10 mm	−	−, 0	−	A	Regular adipocytes
6_control/a		−	−, 1	−	A&S	Vessel, stromal native cells
6_control/b		−	−, 0	−	S	Lipolysis, stromal lipid dispersion (Fig. 2, inset 1)
6_control/c		−	−, 0	−	A&S	Native cells among adipocytes, crystallization
6_experiment/a	On site	+	+, 8	+	A&S	**Angiogenesis**, lipolysis, stromal native cells
6_experiment/b	On site	+	+, >20	+	A&S	**Angiogenesis**, stromal native cells
6_experiment/c	2–5 mm	+/−	+, 7	+	S	Mammary ducts
6_experiment/d	10 mm	−	−, 0	−	A&S	Stromal native cells, collagen production
7_control/a		+/−	+, 13	+	S	**Lymphangiogenesis, non-native cell recruitment** (Fig. 3B)
7_control/b		+/−	−, 5	−	A&S	**Angiogenesis, non-native cell recruitment**, lipolysis, stromal native cells (Fig. 3A)
7_control/c		−	−, 0	−	A	Regular adipocytes
7_experiment/a	On site	+	+, >20	+	A&S	**Non-native cell recruitment, reorganized collagen**, nerve
7_experiment/b	On site	+	+, >20	+	A&S	**Angiogenesis, lymphangiogenesis, reorganized collagen, fibroblast activation**, nerve
7_experiment/c	2–5 mm	+/−	+, 12	+	A&S	Lipolysis, stromal lipid dispersion
7_experiment/e	10 mm	−	−, 5	−	S	Stromal lipid dispersion
8_control/a		−	−, 2	−	A	Native cells among adipocytes
8_control/c		−	−, 0	−	A	Regular adipocytes
8_experiment/a	On site	+	+, 18	+	T/S	**Reorganized collagen**, tumor (cells) (Fig. 3D)
8_experiment/b	2–5 mm	+/−	+, 16	+	A&S	Mammary duct, stromal native cells, lipolysis (Fig. 4, inset 2)

continued on next page

A

Week_rat/ sampling site	Site related to tumor	Visual	Vesicles, count	R3050	Class	Tumor microenvironment events* and other biological structures/events (figure reference)
8_experiment/e	2–5 mm	+/−	+, 16	+	A&S	Lipolysis (Fig. 4, inset 1)
9_control/a		−	−, 1	−	A	Native cells among adipocytes
9_experiment/a	On site	+	−, 1	−	T	Tumor necrosis
9_experiment/b	On site	+	−, 0	−	T	Tumor necrosis
9_experiment/d	2–5 mm	+/−	+, 15	+	A&S	Lipolysis, native cells, deformed adipocytes
9_experiment/f	10 mm	−	−, 2	−	A&S	Stromal native cells, lipolysis

B

Week_rat/ sampling site	Site related to tumor	Visual	Vesicles/R3050	Class	Tumor microenvironment events* and other biological structures/events (figure reference)
7_control/d	10 mm	−	−	A&S	Stromal native cells, lipolysis
7_experiment/d	On site	+	+	A&S	**Lymphangiogenesis, angiogenesis, non-native cell recruitment, reorganized collagen, fibroblast activation, fibrosis**, nerve, blood cells, tumor (cells) (Fig. 1)
8_control/b		−	−	A&S	Native cells (Fig. 2, main)
8_control/d		−	−	A	Regular adipocytes
8_experiment/c	On site	+	+	T&S	**Reorganized collagen, basement membrane degradation, lymphangiogenesis, non-native cell recruitment, angiogenesis**, tumor (cells), native cells
8_experiment/d	On site	+	+	A&S	**Fibroblast activation, fibrosis, angiogenesis, reorganized collagen, non-native cell recruitment**, native cells, lipolysis, tumor cells
9_control/b		−	−	A	Native cells
9_experiment/c	On site	+	−	T	Tumor necrosis
9_experiment/e	2–5 mm	+/−	+	A&S	Lipolysis, native cells, deformed adipocytes (Fig. 4, main)

*Tumor microenvironment events are in bold font.

vessels that have the AF$^{(3)}$-visible vesicles and developed vessels free of these vesicles (Fig. 1). The same type of vesicles appears to initiate both angiogenesis and lymphangiogenesis.

We therefore used this vesicle reporter, rather than the established external labeling that may perturb the tumor microenvironment (37), to visualize (lymph-)angiogenesis throughout our longitudinal study. It should be noted that the observed angiogenesis in ex vivo tissue seems to be rather different from the classic sprouting mechanism of angiogenesis observed in vitro (38). (Lymph-)angiogenesis was widely observed in tumors but was largely absent in nontumor samples (Table 1), except for two samples from the abnormal control rat that seemed to undergo spontaneous angiogenesis (Fig. 3A and 7_control/b in

Table 1A) and lymphangiogenesis (Fig. 3B and 7_control/a in Table 1A). The corresponding histopathology confirmed that this abnormal control rat developed breast cancer spontaneously without carcinogen injection.

Degradation of basement membrane is required for tumor invasion, proliferation, and metastasis (10), and it may be present around blood vessels (Fig. 3B) and lymphatic vessels or mammary ducts/lobules (Fig. 3C). As expected, the basement membrane degradation is absent in nontumor samples (Table 1). In addition to the basement membrane degradation, another form of extracellular matrix reorganization is associated with $\chi^{(2)}_{SHG}$-visible collagen. Tubular collagen reorganization to accommodate angiogenesis can be found at different
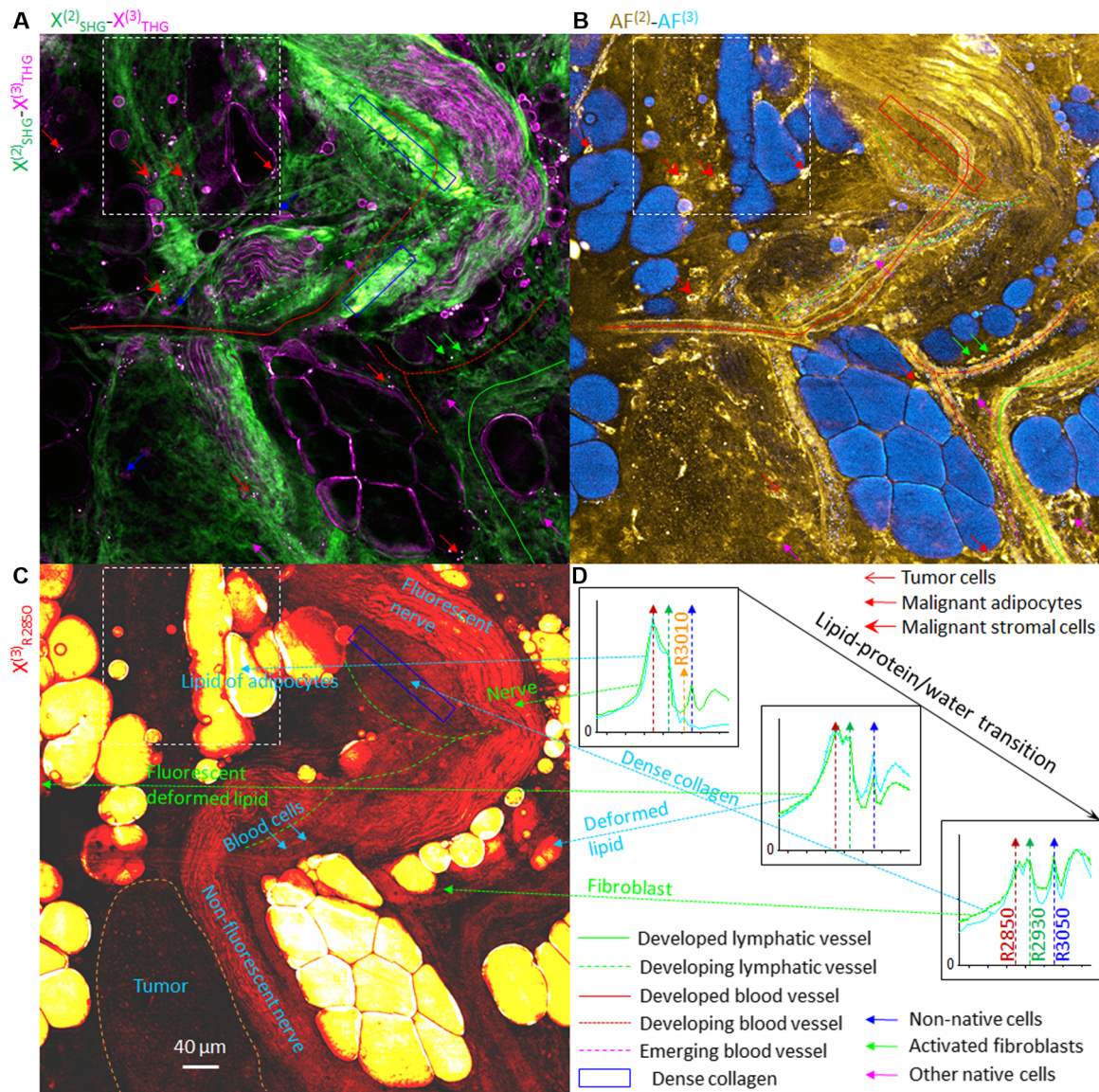
Tu *et al. Sci. Adv.* 2017;**3**:e1600675   25 January 2017

5 of 13

Fig. 1. Coregistered lower dimensional multicontrast images of an unperturbed mammary tumor from a carcinogen-injected rat. (**A**) Composite $\chi^{(2)}_{SHG}$-$\chi^{(3)}_{THG}$ image reflecting local optical structure. (**B**) Composite $AF^{(2)}$-$AF^{(3)}$ image reflecting local autofluorescence activity. (**C**) $\chi^{(3)}_{CARS}$ image at R2850. Comparison with the image at R3050 (see fig. S2A) reflects lipid-protein composition. (**D**) In situ chemical analysis revealing local (9-pixel average, 1.5×1.5 μm^2) lipid-protein/water transition. The $\chi^{(3)}_{CARS}$ spectra in three panels plot $\chi^{(3)}_{CARS}$ intensity (arbitrary unit) against vibration frequency across the R2550-R3250 range. Molecular vibrations corresponding to the observed peaks of R2850, R2930, and R3010 are explicitly shown. In (A) to (C), the lipolytic region marked by broken squares can be directly compared to its counterparts in Figs. 2 and 4. The flow in one developing blood vessel can be visualized (see movie S1).

stages of angiogenesis (Fig. 1A and fig. S2I). In addition, dense collagen known as fibrosis can form in concert with (lymph-)angiogenesis (Fig. 1A) (*11*, *12*).

Fibroblast activation and non-native cell recruitment

An isolated (malignant) cell can be typically recognized as having $AF^{(2)}$-visible (flavin adenine dinucleotide–rich) cytoplasm and a void of optical signal from the nucleus (Figs. 1B, 2B, and 3B) (*28*). Regular collagen production can be recognized from the composite $AF^{(2)}$-$\chi^{(2)}_{SHG}$ image, in which $\chi^{(2)}_{SHG}$-visible collagen fibers are generated along the elongated directions of $AF^{(2)}$-visible fibroblasts (table S4). This dual-contrast imaging can visualize fibroblasts without (frequently un-

specific) external markers (*9*). Rather strikingly, the collagen production may be accompanied by the $AF^{(3)}$-visible angiogenesis along the same directions (Fig. 3D), confirming the role of fibroblast activation in stimulating angiogenesis in tumor development (*9*). The fibroblast activation may have also induced fibrosis in the same field of view (Fig. 3D).

$AF^{(2)}$-visible $\chi^{(3)}_{THG}$-invisible cells, other than the fibroblasts, can be found in nontumor samples and tumors (for example, Figs. 1B and 3E) and are therefore termed generally as native cells. Some cells with high $\chi^{(3)}_{THG}$ contrast but low $AF^{(2)}$ emerge along with the native cells in the $AF^{(2)}$-$\chi^{(3)}_{THG}$ image of a tumor (Fig. 3E). Similar $\chi^{(3)}_{THG}$-visible cells can be found in the sample undergoing spontaneous carcinogenesis
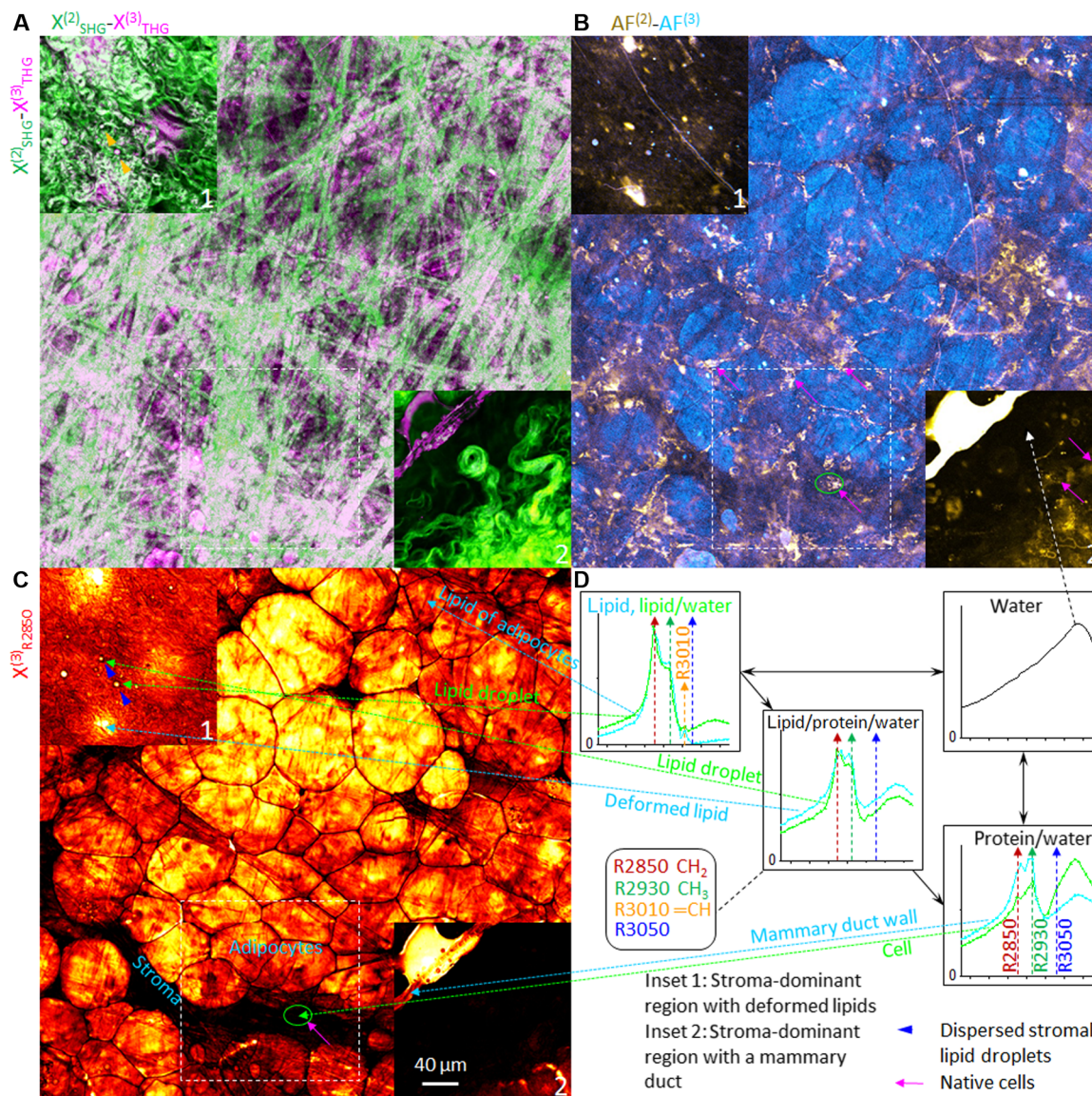
Tu *et al. Sci. Adv.* 2017;**3**:e1600675   25 January 2017

6 of 13

Fig. 2. Coregistered multicontrast images of an unperturbed mammary specimen from a control rat. (**A**) Composite $\chi^{(2)}_{SHG}$-$\chi^{(3)}_{THG}$ image reflecting local optical structure. (**B**) Composite $AF^{(2)}$-$AF^{(3)}$ image reflecting local autofluorescence activity. Regular adipocytes are recognized as $AF^{(2)}$-visible cytoplasm located at the periphery of large $AF^{(3)}$-visible lipid droplets. (**C**) $\chi^{(3)}_{CARS}$ image at R2850. The comparison with the image at R3050 reflects local lipid-protein/water transition. (**D**) In situ chemical analysis revealing local (9-pixel average, 1.5×1.5 μm^2) lipid-protein/water transition. In (A) to (C), the lipolytic region marked by broken squares can be directly compared to its counterparts in Figs. 1 and 4. Inset 1: A stroma-dominant region with stromal lipid dispersion and deformed lipids from mammary specimen of a control rat. Inset 2: Another stroma-dominant region with a mammary duct from normal-appearing mammary specimen of a carcinogen-injected rat.

(Fig. 3, A and B) and other tumor samples (for example, Fig. 3C), but not in nontumor samples (table S4). Thus, these cells are not native to the normal mammary gland and can be treated as a cancer indicator. This observation is consistent with the recruitment of non-native immune cells (7) or bone marrow–derived cells (8) in carcinogenesis.

Metabolic switch identified by in situ chemical analysis

Lipolysis and lipid breakdown result in a lipid-protein/water transition that decreases lipid content and increases protein/water content (table S4). They can be recognized in the hyperspectral $\chi^{(3)}_{CARS}$ image stack that consists of a sequence of $\chi^{(3)}_{CARS}$ images, in which each pixel reflects an entire $\chi^{(3)}_{CARS}$ spectrum that indicates chemical content in

situ (Figs. 1D, 2D, and 4D) (31, 39). Altered metabolism along the lipid-protein/water transition, which manifests itself as an elevated ratio of $\chi^{(3)}_{R2930}/\chi^{(3)}_{R2850}$, has been used to detect the tumor margin of breast cancer (31) and brain cancer (32). Similar ratiometric indicators have been widely used in diagnostic Raman spectroscopy. However, it should be noted that this ratio alone is not a reliable cancer indicator because the lipolysis and lipid breakdown that elevate this ratio are not specific to tumors (Figs. 1D, 2D, and 4D and table S4). In particular, the nonadipocyte stromal regions (Fig. 2, insets 1 and 2) that occupy ~20% of the field of view of nontumor samples (Fig. 2, main) have a high ratio and may thus be mistakenly treated as tumorous regions.
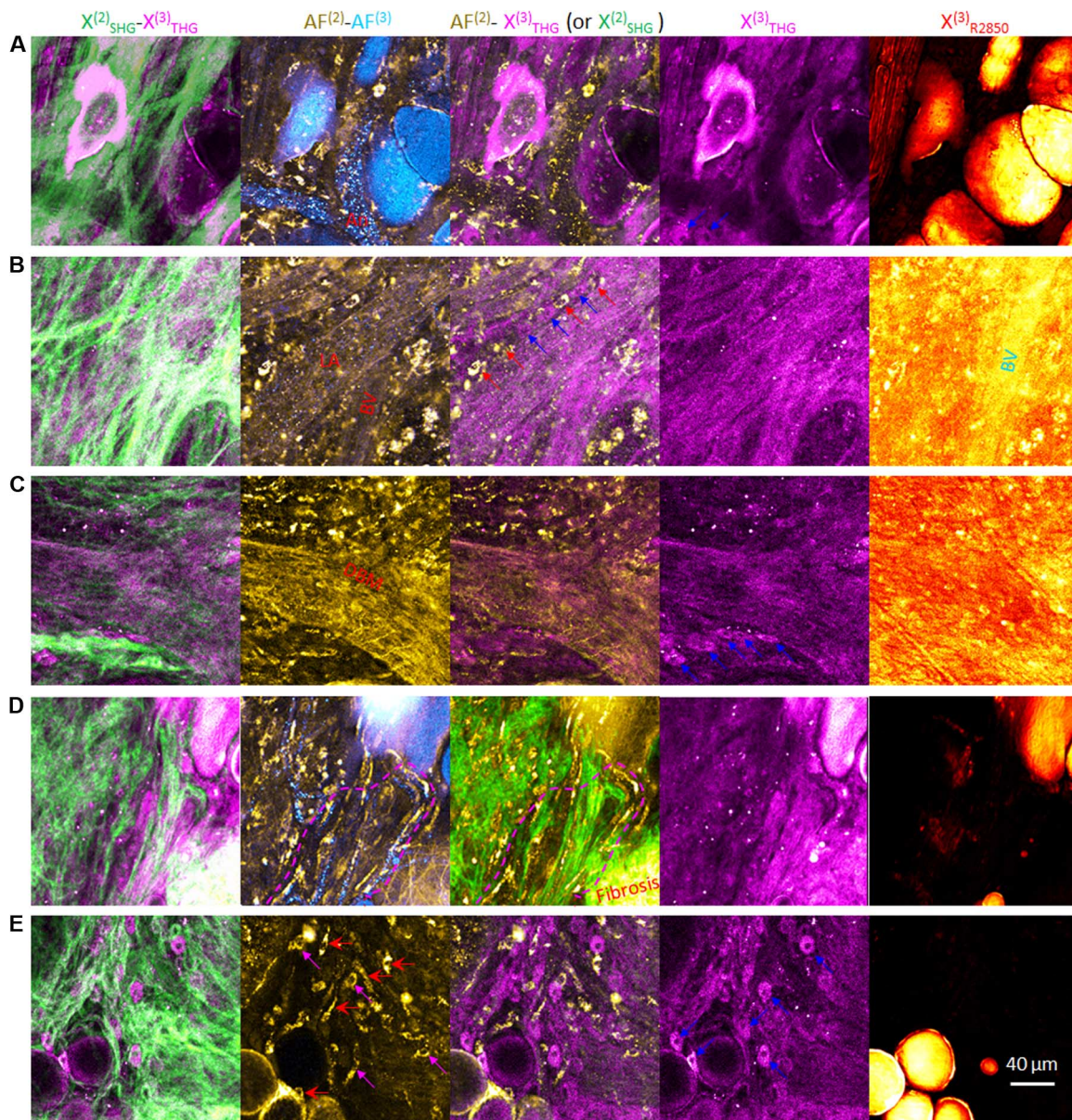
Fig. 3. Macroscopic events in the tumor microenvironment identified by multicontrast imaging. Each image contains 380 × 380 pixels with 0.5-μm pixel size. (**A**) Natural angiogenesis (An). (**B**) Lymphangiogenesis (LA) near a blood vessel (BV), which can be differentiated from the LA by the presence of $\chi^{(3)}_{R2850}$ contrast. Some native cells (red arrows) and non-native cells (blue arrows) are also marked. (**C**) Degraded basement membrane (DBM) from lymphatic vessels or mammary ducts/lobules. Some non-native cells (blue arrows) are also marked. (**D**) Collagen production and fibroblast activation demonstrated by paralleled formation of fibroblasts, collagen fibers, and angiogenic vessels (area marked by broken magenta line). A fibrosis feature of dense collagen is also identified. (**E**) Non-native cell recruitment. Tumor cells (red arrows), nontumor native stromal cells (magenta arrows), and non-native cells (blue arrows) can be discriminated against each other according to $\chi^{(3)}_{THG}$ contrast and $\chi^{(3)}_{THG}$-AF$^{(2)}$–covisible tumor-associated extracellular vesicles.

In contrast, a closely related on-and-off (nonratiometric) cancer indicator can be found within the detectable CH-stretch Raman range across R2550-R3250. Except for the regions of adipocytes free of the lipid-protein/water transition (cyan curves in upper panels of Figs. 1D, 2D, and 4D), this indicator presents as an emergent R3050 peak in the $\chi^{(3)}_{CARS}$ spectra of tumor or precancerous samples, but not in nontumor samples, independent of the sampling location (pixel) of the in situ chemical analysis (Figs. 1D, 2D, and 4D). For example, the protein-rich cells (or mammary duct wall) in the spatially precancerous sample of Fig. 4 (main or inset 2) can be discriminated against their

counterparts in the nontumor sample of Fig. 2 (main or inset 2) by simply detecting this R3050 peak (Figs. 2D and 4D, lower panels). The same biomarker has also differentiated other features with varying degrees of lipid-protein/water transition (deformed adipocytes, lipid droplets, peripheral nerves, vasculature walls or boundaries, fibroblasts, collagen-rich stromal regions, stromal fluids, etc.) in the tumor and (temporally or spatially) precancerous samples from their nontumor counterparts (Table 1A).

The R3050 peak is present in tumor-specific regions of fibrosis (Fig. 1D, lower panel) and (lymph-)angiogenesis that are rich in protein and
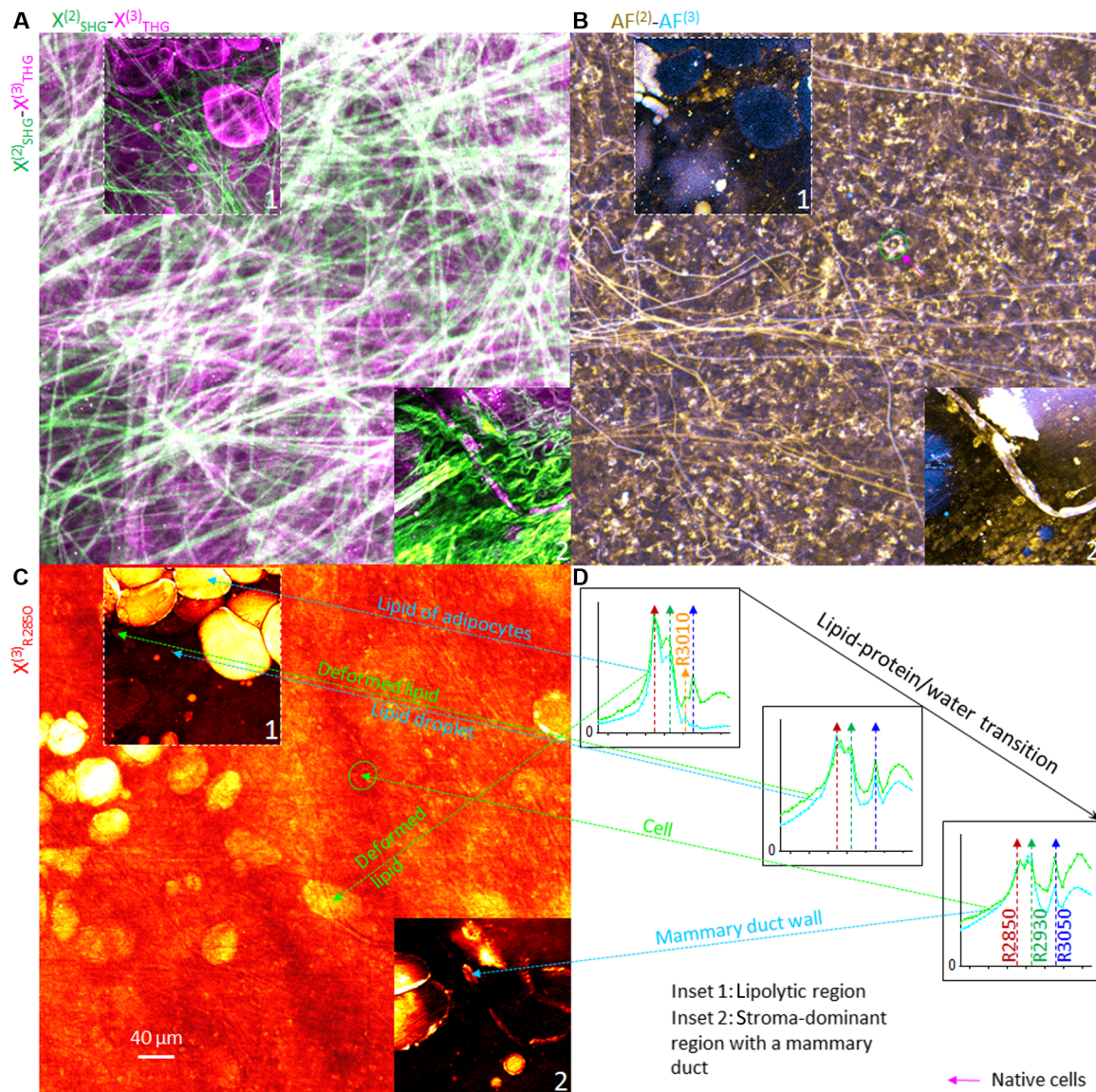
Tu *et al. Sci. Adv.* 2017;**3**:e1600675   25 January 2017

8 of 13

Fig. 4. Coregistered multicontrast images of an unperturbed precancerous mammary specimen from a carcinogen-injected rat. (**A**) Composite $\chi^{(2)}_{SHG}$-$\chi^{(3)}_{THG}$ image reflecting local optical structure. Enriched $\chi^{(3)}_{THG}$-AF$^{(2)}$–covisible tumor-associated extracellular vesicles are found in contrast to the control sample of Fig. 2A. (**B**) Composite AF$^{(2)}$-AF$^{(3)}$ image reflecting local autofluorescence activity. In contrast to the tumor or malignant cells in Fig. 1B, none of the AF$^{(2)}$-visible cells seems to have more than one of these vesicles inside the cell body. They are likely deformed adipocytes that are accepting these vesicles (see movie S2). (**C**) $\chi^{(3)}_{CARS}$ image at R2850. The comparison with the image at R3050 reflects local lipid-protein/water transition. (**D**) In situ chemical analysis revealing local (9-pixel average, $1.5 \times 1.5 \ \mu m^2$) lipid-protein/water transition. Inset 1: Lipolytic region with deformed lipids and lipid breakdown from precancerous mammary specimen of another carcinogen-injected rat. This broken square–marked region can be directly compared to its counterparts in Figs. 2 and 3, indicating that the differences between the tumor (or precancerous) and nontumor samples are the enrichment of the tumor-associated extracellular vesicles and the emergence of the R3050 peak, just like the comparison between the main parts of Figs. 2 and 4. Inset 2: Stroma-dominant region with a mammary duct near the region of inset 1, which can be directly compared to inset 2 in Fig. 2 to reveal the same differences.

water and also in skin and muscle specimens resected from the control animals, suggesting that up-regulated water-soluble molecules from biosynthesis (for example, amino acids, peptides, and low–molecular weight proteins) are responsible for this spectral peak. Consistently, the R3050 peak disappears whenever biosynthesis-inactive large lipid droplets are probed (Fig. 1D, upper panel) or when tumor cells undergo necrosis with no active biosynthesis (Table 1A). Thus, the emergence of the R3050 peak reflects a metabolic switch from an energy-storing phenotype of normal mammary gland to a biosynthesis phenotype found in regular skin and muscle (17). In comparison to other animal cancer models of skin or other biosynthesis-active organs, the unique absence of the biosynthesis phenotype in prepuberty mammary gland (our selected animal model) enables sensitive detection of this metabolic switch.

Interrelated microscopic and macroscopic events in the tumor microenvironment

With the simultaneous observation of macroscopic and microscopic tumor microenvironment events (7–17) in tumors and precancerous samples (Table 1), it is now possible to investigate their interrelationships

in this longitudinal study. Once a cutoff density of tumor-associated extracellular vesicles (six per field of view) is chosen to differentiate tumor/precancerous samples from nontumor samples, this vesicle-based cancer indicator and the R3050 biomarker become self-consistent (Table 1A). The two microscopic events (extracellular vesicle enrichment and metabolic switch) cross-validate one another and assert quantitatively that the two temporally precancerous samples and six spatially precancerous samples from carcinogen-injected rats that appear uncertain on visual inspection ("+/−" in Table 1A) are in early stages of carcinogenesis. A spectroscopic cancer indicator, such as the R3050 biomarker, may be of clinical significance during intraoperative surgery, in which visual inspection could be unreliable (32).

Throughout tumor development before necrosis, at least one of the three macroscopic tumor microenvironment events was observed in 13 of 15 tumor samples, but in 0 of 6 spatially precancerous samples and 0 of 2 temporally precancerous samples (Table 1A). Because the two microscopic tumor microenvironment events were universally observed in these samples, in contrast to the nontumor samples, the disparate distribution of the macroscopic events in the tumor and precancerous samples (for example, compare Fig. 4 with Fig. 1) strongly suggests a causal relation from the microscopic events to the macroscopic events. That is, the extracellular vesicle enrichment and metabolic switch may directly cause the subsequent large-scale changes of non-native cell recruitment or fibroblast activation, extracellular matrix reorganization, and (lymph-)angiogenesis. The only exception to this hypothesis is the unique sample from the abnormal control rat (7_control/b in Table 1A), which showed that angiogenesis preceded the two microscopic events. We speculate that this natural angiogenesis provided a favorable environment to induce the two microscopic events revealed in another sampling site (7_control/a in Table 1A) and subsequently cause spontaneous carcinogenesis. Except for this nontrivial sample and two trivial samples with necrosis, there is a full agreement between the two cross-validated cancer indicators and visual inspection (Table 1A).

Because of the known extracellular communication functions of extracellular vesicles (40), the possible sequence of the observed events is as follows: (i) sparse tumor cells release the extracellular vesicles to modulate their surrounding microenvironment inside the mammary organ; (ii) numerous fibroblasts, adipocytes, and other native cells accept the vesicles and switch their metabolism from energy production and storage to biosynthesis; (iii) the metabolic switch induces the non-native cell recruitment, extracellular matrix reorganization, and (lymph-)angiogenesis to produce the tumor microenvironment we currently understand (7–15).

Applicability to human breast cancer

Because no specific sample treatment is required for these investigations, we readily imaged fresh sections of human breast cancer to detect the tumor-associated extracellular vesicles. Various vesicles were found in a biopsied specimen of human breast tumor with prominent lipolysis (Fig. 5A) and can be classified into three distinct classes with different cross-contrast visibility (Fig. 5B). The in situ chemical analysis indicates that one class of eight $\chi^{(3)}_{THG}$-$AF^{(3)}$–covisible vesicles have a protein-like spectrum (Fig. 5C) similar to the spectrum of their rat counterparts and are absent in the normal tissue from the same patient (fig. S3). The other two classes, including one with 173 $AF^{(2)}$-$AF^{(3)}$–covisible vesicles, have strong $AF^{(2)}$ signals and lipid-like spectra (Fig. 5D). They are likely derived from the lipids of adipocytes (for example, area β; Fig. 5A). Because the spectrum of either class of vesicles approximates that of the surrounding interstitial fluid (area α; Fig. 5A), they are $\chi^{(3)}_{CARS}$-invisible due to low contrast. Despite this invisibility, the cross-contrast

imaging beyond $\chi^{(3)}_{CARS}$ allows in situ chemical analysis to discriminate between the two. Thus, the three classes of vesicles found in the human breast cancer tissue can all be correlated with those found in the rat mammary tumors (table S3). These results reinforce the applicability of vesicle-based cancer indicators in human breast cancer. More detailed studies are needed to determine whether this vesicle enrichment is a more universal process in the early development of other cancers as well (41).

DISCUSSION

The metabolic switch toward biosynthesis (17) is typically treated as an adaptation to a stressed tumor microenvironment (18), that is, a consequence of macroscopic events such as the extracellular matrix reorganization. Somewhat surprisingly, the evidence provided here suggests that this metabolic switch occurs in both temporally and spatially precancerous samples and can precede extracellular matrix reorganization and other macroscopic events in the tumor microenvironment. The observation of the metabolic switch during the earliest stages of tumor development reinforces the notion to classify it as an emerging hallmark of cancer (42).

The in vivo role of extracellular vesicles has been relatively elusive without observing them label-free in tissue. By visualizing these vesicles in situ in the unperturbed tumor microenvironment, we have found a direct link between their enrichment and the metabolic switch toward biosynthesis. Thus, these vesicles may serve as the signaling mediators from the tumor cells to the abundant stromal cells to initiate the metabolic switch, which may, in turn, induce various macroscopic events in the tumor microenvironment. Genetic modification of the stromal cells can occur when they accept the vesicles with RNA (43). These observations establish the extracellular vesicle enrichment as a fundamental tumor microenvironment event worthy of further investigation.

Both the metabolic switch and the extracellular vesicle enrichment are microscopic events in the tumor microenvironment and are independent of the macroscopic heterogeneity of the sample. This aspect, together with their concurrence at the earliest stages of tumor development, may qualify them as more effective targets for cancer diagnosis and therapeutic intervention (16, 17) than the subsequent macroscopic events. Their concurrence in the precancerous regions may have clinical significance during intraoperative procedures, suggesting that the tumor margin may actually lie well beyond the visually delineated structural tumor boundary that is currently defined histologically.

We note that the major conclusions in this study are drawn from a rather small-scale animal study. In addition, the applicability to human study has been limited to a few specimens. The recognition of various macroscopic tumor microenvironment events is based on morphological features and therefore subjective to interobserver variations. These limitations can be overcome by future large-scale animal and human studies and the development of machine learning procedures to automatically recognize the events.

The simultaneous observation of both microscopic and macroscopic events in these unperturbed tumor microenvironments highlights the advantage of our multicontrast imaging methodology in cancer research and for future assessment of therapeutic strategies. These complex events in carcinogenesis and metastasis could not be easily detected if investigated by only one individual contrast mechanism or imaging modality, or with a lower dimension of combined contrast mechanisms. With these multiple contrasts, malignant cells
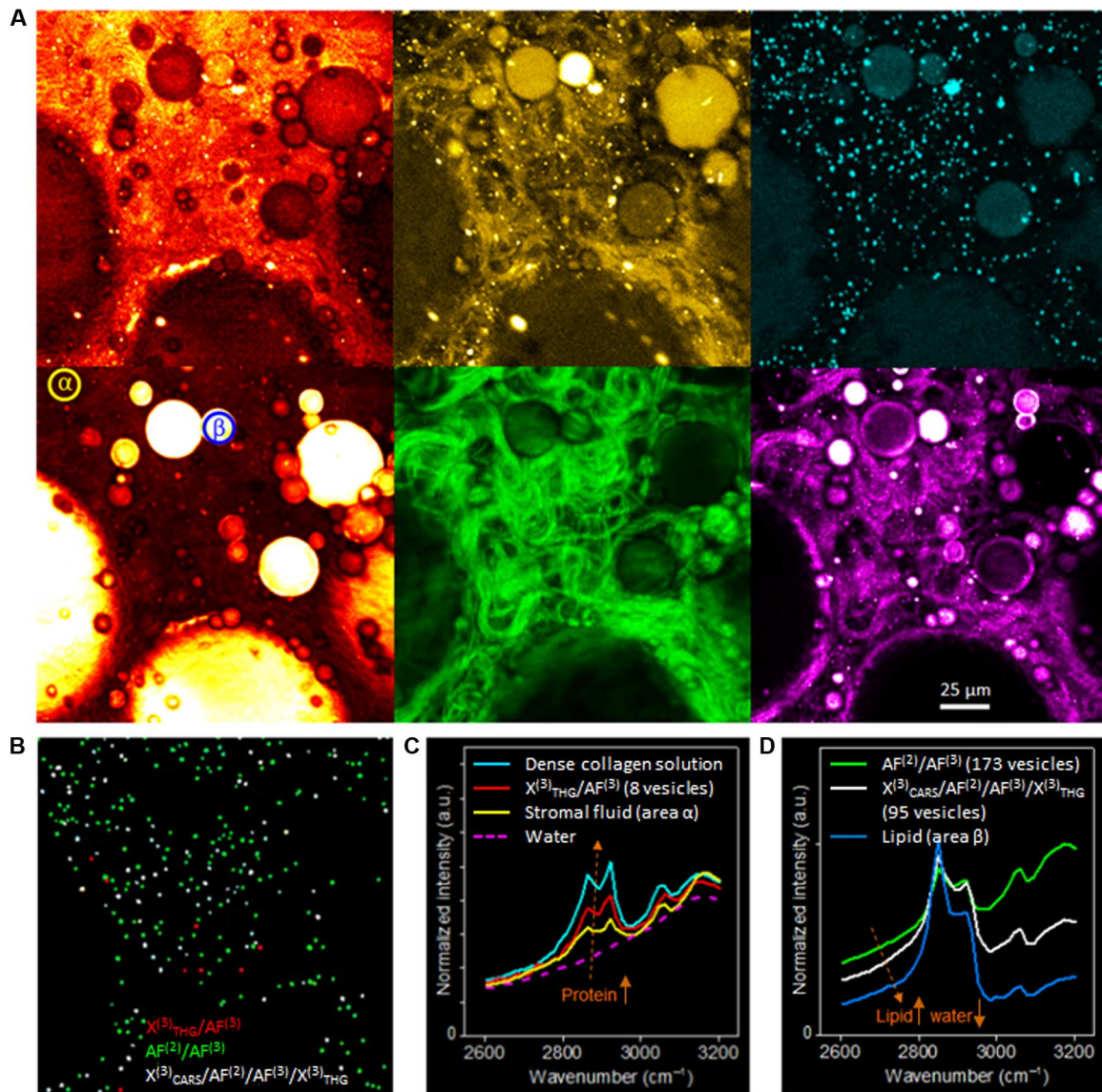
Fig. 5. Coregistered single-contrast images of an unperturbed human mammary tumor with various extracellular vesicles. (**A**) Multicontrast images of different pseudocolor representations. Red, $\chi^{(3)}_{R3050}$ (upper left) or $\chi^{(3)}_{R2850}$ (lower left); yellow, $AF^{(2)}$; green, $\chi^{(2)}_{SHG}$; cyan, $AF^{(3)}$; magenta, $\chi^{(3)}_{THG}$. Area α represents interstitial fluid consisting of a dilute protein solution, whereas area β is a lipid with high $AF^{(2)}$ signal. (**B**) Distribution of three distinct classes of vesicles (276 vesicles) automatically identified by a software algorithm [that quantifies the prominence of a vesicle and its full-width half-maximum (FWHM) size] and classified by cross-contrast visibility. (**C**) $\chi^{(3)}_{CARS}$ spectra of pure water, the interstitial fluid in area α, one class of vesicles averaged over eight vesicles, and a dense collagen region indicative of a progressive increase of protein content in water. Data from water and the dense collagen region are from other independent experiments. a.u., arbitrary units. (**D**) $\chi^{(3)}_{CARS}$ spectra of the lipid in area β and the other two classes of vesicles indicative of a progressive increase of lipid/water ratio.

and angiogenic vessels can be respectively "labeled" by intrinsic tumor-associated vesicles and tubularly aligned vesicles to differentiate them from normal cells and regular blood vessels. A wide variety of other features in carcinogenesis can also be similarly identified. The use of more invasive exogenous labeling, specific sample treatment, and genetic modification are no longer required to attain this level of imaging so that any associated artifacts are avoided. This investigational approach and visualization methodology is possible in the unperturbed tumor microenvironment, enabling the study of the complex dynamics and spatially and temporally resolved characteristics of tumor cells and tumor-associated extracellular vesicles, with future applications in in vivo preclinical animal tumor models and in clinical human studies.

MATERIALS AND METHODS
Animal and human tissues
Animal procedures were conducted under a protocol approved by the Institutional Animal Care and Use Committee at the University of Illinois Urbana-Champaign. A total of 20 female rats (F344, Harlan) were included in the study, with 10 carcinogen-injected and 10 control animals. Mammary tumors were induced in 7-week-old rats by intra-peritoneal injection of *N*-nitroso-*N*-methylurea (NMU; Sigma-Aldrich) at a concentration of 55 mg/kg. The first injection was administered on the left abdominal side, followed by a second injection 1 week later on the right abdominal side. This NMU-induced rat mammary tumor model is well established and particularly suitable for investigating

breast cancer development because the anatomical and pathological features, the hormone dependency, and the immunohistochemical responses of the lesions mimic human ductal carcinoma in situ (44–46). The tumors were first palpable from the abdominal surface approximately 4 weeks after the second injection (Table 1). For the control group, an equal amount of saline was injected to account for any effects from the injection alone. The rats from both groups were euthanized 1 to 9 weeks after the second injection (Table 1). Mammary tissue was dissected and placed in saline at 4°C before imaging within 12 hours.

Human tissue was obtained under a protocol approved by the institutional review boards at the University of Illinois at Urbana-Champaign and Carle Foundation Hospital. After surgical removal, excess cancerous and normal breast tissue from a patient was stored in saline-filled conical tubes and transported on ice for imaging within 12 hours.

Pulse-shaping multiphoton microscope

The short-wavelength edge of the generated supercontinuum (780 to 880 nm) (47) was reflected by a dichroic mirror (DMLP900, Thorlabs) as the pump beam for CARS, whereas the main supercontinuum (900 to 1300 nm) was sent into a commercial pulse shaper as the CARS Stokes beam or the excitation beam to generate the contrast from $AF^{(2)}$, $AF^{(3)}$, $\chi^{(2)}_{SHG}$, or $\chi^{(3)}_{THG}$ (fig. S1). The Stokes beam was optically delayed by a computer-controlled delay line to realize spectral focusing CARS (48) and collect the vibrational contrast of $\chi^{(3)}_{CARS}$. Two SF57 glass blocks were placed in the pump/Stokes beams to prechirp the pulses. The two beams were then recombined by another dichroic mirror, steered into a commercial microscope (BX61WI, Olympus), and focused by a super-apochromat objective (UPLSAPO 60×W/IR; numerical aperture, 1.20; Olympus). In $AF^{(2)}$/$AF^{(3)}$/$\chi^{(2)}_{SHG}$/$\chi^{(3)}_{THG}$ imaging, the CARS pump beam was blocked by a computer-controlled shutter (fig. S1). A pixelated $4f$ pulse shaper (MIIPS Box640, Biophotonic Solutions) was used to iteratively compress the supercontinuum pulse, whereas the pulse measurement based on multiphoton intrapulse interference phase scans (MIIPS) (49) was used in the iteration loop. The coherence of the supercontinuum was validated by the converged iteration toward transform-limited pulse compression. The technique of "local compression" (47) was used to generate tunable ~30-fs pulses across the bandwidth of the supercontinuum. After the transform-limited pulse compression, the pulses were programmed for customized multiphoton imaging modalities.

Label-free nonlinear optical imaging with multiple contrasts

The excitation pulses customized for the multiple imaging modalities were amplitude/phase-shaped from the supercontinuum and paired with various detection filters to target different endogenous molecules or structures of interest. The incident power of the phase-shaped supercontinuum pulses was attenuated by amplitude shaping to conservatively safe levels (table S1) so that no sample damage was observed and the same sample could be repeatedly imaged by different modalities. To validate the multiphoton imaging modalities, we performed power dependence tests for each modality with the unstained cancerous and normal rat mammary tissue. Images (380 × 380 pixels, 0.5 × 0.5 μm^2 per pixel) were acquired with different average powers, and the average intensity (photon counts) was calculated and plotted against excitation average powers on double logarithmic scales. The linearly fitted slopes were consistent with the quadratic power dependence for $AF^{(2)}$ and $\chi^{(2)}_{SHG}$, the cubic power dependence for $AF^{(3)}$ and $\chi^{(3)}_{THG}$, and the quadratic/linear power dependence in pump/Stokes for $\chi^{(3)}_{CARS}$.

The small deviation from the theoretical numbers (<10%) might be due to the diverse biomolecular composition of the tissue samples, excitation/emission cross-talk, and low or saturated signal within the field of view.

Image acquisition was performed by raster scanning a piezoelectric stage with a pixel dwell time of 200 μs for all modalities. To generate a strong and high–spectral resolution $\chi^{(3)}_{CARS}$ signal, the spectrally dispersive power of the supercontinuum was concentrated into a single vibrational frequency by spectral focusing, in which both the pump and Stokes pulses were chirped so that their instantaneous frequency difference remained the same during their interaction time to coherently drive one molecular vibration (48). Spectroscopic acquisition was achieved by scanning the delay between two pulses to tune the frequency difference with a spectral resolution of 14 cm^{-1}, which was calculated from the measured FWHM (19 cm^{-1}) of the 2913-cm^{-1} peak in the $\chi^{(3)}_{CARS}$ spectrum of dimethyl sulfoxide. This spectral-focusing CARS was used to collect hyperspectral CARS images from the biological samples, each of which was obtained at one Raman vibration frequency that was varied among the images. The $\chi^{(3)}_{CARS}$ spectrum at an arbitrarily selected region of interest was calculated from these images over the corresponding pixels. The $\chi^{(3)}_{CARS}$ spectrum from a single-pixel adipocyte region in a normal human breast tissue approximated that of a larger 500-pixel adipocyte region with sufficient signal-to-noise ratio (fig. S3). Similar calculations were used to obtain the local $\chi^{(3)}_{CARS}$ spectra in other features. In both human and animal tissues, a thick section was placed on a microscope slide and sealed under a coverslip. The imaging focal plane was placed ~10 μm below the sample surface.

SUPPLEMENTARY MATERIALS

table S1. Multicontrast nonlinear imaging to observe various tumor microenvironment events.
table S2. New knowledge acquisition by dimension-increased multicontrast image analysis of a rat mammary tumor.
table S3. Observed micrometer-sized vesicles in mammary tissue classified by cross-contrast visibility and chemical content.
table S4. Macroscopic events observed in tumor microenvironments and in nontumor mammary samples.
fig. S1. Schematic for label-free multicontrast nonlinear imaging.
fig. S2. Coregistered multicontrast images of an unperturbed mammary tumor from a carcinogen-injected rat.
fig. S3. Coregistered single-contrast images of an unperturbed normal human mammary specimen.
movie S1. Sweeping of hyperspectral $\chi^{(3)}_{CARS}$ images from the middle-right corner of Fig. 1C.
movie S2. Comparison of coregistered multicontrast images from the adipocyte-dominant control mammary tissue sample (Fig. 2, main) and the precancerous mammary sample (Fig. 4, main).

REFERENCES AND NOTES

1. D. Hanahan, R. A. Weinberg, The hallmarks of cancer. *Cell* **100**, 57–70 (2000).
2. L. A. Liotta, E. C. Kohn, The microenvironment of the tumour–host interface. *Nature* **411**, 375–379 (2001)
3. M. J. Bissell, D. Radisky, Putting tumours in context. *Nat. Rev. Cancer* **1**, 46–54 (2001).
4. I. J. Fidler, The pathogenesis of cancer metastasis: The 'seed and soil' hypothesis revisited. *Nat. Rev. Cancer* **3**, 453–458 (2003).
5. M. M. Mueller, N. E. Fusenig, Friends or foes—Bipolar effects of the tumour stroma in cancer. *Nat. Rev. Cancer* **4**, 839–849 (2004).
6. J. A. Joyce, J. W. Pollard, Microenvironmental regulation of metastasis. *Nat. Rev. Cancer* **9**, 239–252 (2009).
7. H. F. Dvorak, Tumors: Wounds that do not heal. Similarities between tumor stroma generation and wound healing. *N. Engl. J. Med.* **315**, 1650–1659 (1986).
8. A. E. Karnoub, A. B. Dash, A. P. Vo, A. Sullivan, M. W. Brooks, G. W. Bell, A. L. Richardson, K. Polyak, R. Tubo, R. A. Weinberg, Mesenchymal stem cells within tumour stroma promote breast cancer metastasis. *Nature* **449**, 557–563 (2007).

9. A. Orimo, P. B. Gupta, D. C. Sgroi, F. Arenzana-Seisdedos, T. Delaunay, R. Naeem, V. J. Carey, A. L. Richardson, R. A. Weinberg, Stromal fibroblasts present in invasive human breast carcinomas promote tumor growth and angiogenesis through elevated SDF-1/CXCL12 secretion. *Cell* **121**, 335–348 (2005).

10. R. Kalluri, Basement membranes: Structure, assembly and role in tumour angiogenesis. *Nat. Rev. Cancer* **3**, 422–433 (2003).

11. K. R. Levental, H. Yu, L. Kass, J. N. Lakins, M. Egeblad, J. T. Erler, S. F. T. Fong, K. Csiszar, A. Giaccia, W. Weninger, M. Yamauchi, D. L. Gasser, V. M. Weaver, Matrix crosslinking forces tumor progression by enhancing integrin signaling. *Cell* **139**, 891–906 (2009).

12. P. P. Provenzano, K. W. Eliceiri, J. M. Campbell, D. R. Inman, J. G. White, P. J. Keely, Collagen reorganization at the tumor-stromal interface facilitates local invasion. *BMC Med.* **4**, 38 (2006).

13. P. Carmeliet, R. K. Jain, Angiogenesis in cancer and other diseases. *Nature* **407**, 249–257 (2000).

14. S. M. Weis, D. A. Cheresh, Tumor angiogenesis: Molecular pathways and therapeutic targets. *Nat. Med.* **17**, 1359–1370 (2011).

15. S. A. Stacker, M. G. Achen, L. Jussila, M. E. Baldwin, K. Alitalo, Lymphangiogenesis and cancer metastasis. *Nat. Rev. Cancer* **2**, 573–583 (2002).

16. S. EL Andaloussi, I. Mäger, X. O. Breakefield, M. J. A. Wood, Extracellular vesicles: Biology and emerging therapeutic opportunities. *Nat. Rev. Drug Discov.* **12**, 347–357 (2013).

17. M. G. Vander Heiden, L. C. Cantley, C. B. Thompson, Understanding the Warburg effect: The metabolic requirements of cell proliferation. *Science* **324**, 1029–1033 (2009).

18. R. A. Cairns, I. S. Harris, T. W. Mak, Regulation of cancer cell metabolism. *Nat. Rev. Cancer* **11**, 85–95 (2011).

19. T. F. Massoud, S. S. Gambhir, Molecular imaging in living subjects: Seeing fundamental biological processes in a new light. *Genes Dev.* **17**, 545–580 (2003).

20. R. Weissleder, M. J. Pittet, Imaging in the era of molecular oncology. *Nature* **452**, 580–589 (2008).

21. R. Weissleder. V. Ntziachristos, Shedding light onto live molecular targets. *Nat. Med.* **9**, 123–128 (2003).

22. H. F. Zhang, K. Maslov, G. Stoica, L. V. Wang, Functional photoacoustic microscopy for high-resolution and noninvasive in vivo imaging. *Nat. Biotechnol.* **24**, 848–851 (2006).

23. B. J. Vakoc, R. M. Lanning, J. A. Tyrrell, T. P. Padera, L. A. Bartlett, T. Stylianopoulos, L. L. Munn, G. J. Tearney, D. Fukumura, R. K. Jain, B. E. Bouma, Three-dimensional microscopy of the tumor microenvironment in vivo using optical frequency domain imaging. *Nat. Med.* **15**, 1219–1223 (2009).

24. E. Brown, T. McKee, E. diTomaso, A. Pluen, B. Seed, Y. Boucher, R. K. Jain, Dynamic imaging of collagen and its modulation in tumors in vivo using second-harmonic generation. *Nat. Med.* **9**, 796–800 (2003).

25. J. Condeelis. J. E. Segall, Intravital imaging of cell movement in tumours. *Nat. Rev. Cancer* **3**, 921–930 (2003).

26. S. Maiti, J. B. Shear, R. M. Williams, W. R. Zipfel, W. W. Webb, Measuring serotonin distribution in live cells with three-photon excitation. *Science* **275**, 530–532 (1997).

27. W. R. Zipfel, R. M. Williams, R. Christie, A. Y. Nikitin, B. T. Hyman, W. W. Webb, Live tissue intrinsic emission microscopy using multiphoton-excited native fluorescence and second harmonic generation. *Proc. Natl. Acad. Sci. U.S.A.* **100**, 7075–7080 (2003).

28. M. C. Skala, K. M. Riching, A. Gendron-Fitzpatrick, J. Eickhoff, K. W. Eliceiri, J. G. White, N. Ramanujam, In vivo multiphoton microscopy of NADH and FAD redox states, fluorescence lifetimes, and cellular morphology in precancerous epithelia. *Proc. Natl. Acad. Sci. U.S.A.* **104**, 19494–19499 (2007).

29. C. Evans, X. S. Xie, Coherent anti-Stokes Raman scattering microscopy: Chemical imaging for biology and medicine. *Annu. Rev. Anal. Chem.* **1**, 883–909 (2008).

30. E. B. Brown, R. B. Campbell, Y. Tsuzuki, L. Xu, P. Carmeliet, D. Fukumura, R. K. Jain, In vivo measurement of gene expression, angiogenesis and physiological function in tumors using multiphoton laser scanning microscopy. *Nat. Med.* **7**, 864–868 (2001).

31. P. D. Chowdary, Z. Jiang, E. J. Chaney, W. A. Benalcazar, D. L. Marks, M. Gruebele, S. A. Boppart, Molecular histopathology by spectrally reconstructed nonlinear interferometric vibrational imaging. *Cancer Res.* **70**, 9562–9569 (2010).

32. M. Ji, D. A. Orringer, C. W. Freudiger, S. Ramkissoon, X. Liu, D. Lau, A. J. Golby, I. Norton, M. Hayashi, N. Y. R. Agar, G. S. Young, C. Spino, S. Santagata, S. Camelo-Piragua, K. L. Ligon, O. Sagher, X. S. Xie, Rapid, label-free detection of brain tumors with stimulated Raman scattering microscopy. *Sci. Transl. Med.* **5**, 201ra119 (2013).

33. B. Weigelin, G.-J. Bakker, P. Friedl, Intravital third harmonic generation microscopy of collective melanoma cell invasion: Principles of interface guidance and microvesicle dynamics. *Intravital* **1**, 32–43 (2012).

34. H. Chen, H. Wang, M. N. Slipchenko, Y. Jung, Y. Shi, J. Zhu, K. K. Buhman, J.-X. Cheng, A multimodal platform for nonlinear optical microscopy and microspectroscopy. *Opt. Express* **17**, 1282–1290 (2009).

35. S. Sukumar, V. Notario, D. Martin-Zanca, M. Barbacid, Induction of mammary carcinomas in rats by nitroso-methylurea involves malignant activation of H-ras-1 locus by single point mutations. *Nature* **306**, 658–661 (1983).

36. D. Débarre, W. Supatto, A.-M. Pena, A. Fabre, T. Tordjmann, L. Combettes, M.-C. Schanne-Klein, E. Beaurepaire, Imaging lipid bodies in cells and tissues using third-harmonic generation microscopy. *Nat. Methods* **3**, 47–53 (2006).

37. D. M. McDonald, P. L. Choyke, Imaging of angiogenesis: From microscope to clinic. *Nat. Med.* **9**, 713–725 (2003).

38. J. Folkman, C. Haudenschild, Angiogenesis in vitro. *Nature* **288**, 551–556 (1980).

39. C. H. Camp Jr., Y. J. Lee, J. M. Heddleston, C. M. Hartshorn, A. R. Hight Walker, J. N. Rich, J. D. Lathia, M. T. Cicerone. High-speed coherent Raman fingerprint imaging of biological tissues. *Nat. Photonics* **8**, 627–634 (2014).

40. V. Muralidharan-Chari, J. W. Clancy, A. Sedgwick, C. D'Souza-Schorey, Microvesicles: Mediators of extracellular communication during cancer progression. *J. Cell Sci.* **123**, 1603–1611 (2010).

41. E. Cocucci, G. Racchetti, J. Meldolesi, Shedding microvesicles: Artefacts no more. *Trends Cell Biol.* **19**, 43–51 (2009).

42. D. Hanahan, R. A. Weinberg, The hallmarks of cancer: The next generation. *Cell* **144**, 646–674 (2011).

43. J. Skog, T. Würdinger, S. van Rijn, D. H. Meijer, L. Gainche, W. T. Curry Jr., B. S. Carter, A. M. Krichevsky, X. O. Breakefield, Glioblastoma microvesicles transport RNA and proteins that promote tumour growth and provide diagnostic biomarkers. *Nat. Cell Biol.* **10**, 1470–1476 (2008).

44. B. M. Arafah, H. M. Finegan, J. Roe, A. Manni, O. H. Pearson, Hormone dependency in N-nitrosomethylurea-induced rat mammary tumors. *Endocrinology* **111**, 584–588 (1982).

45. K. A. Crist, B. Chaudhuri, S. Shivaram, P. K. Chaudhuri, Ductal carcinoma in situ in rat mammary gland. *J. Surg. Res.* **52**, 205–208 (1992).

46. M. Singh, J. N. McGinley, H. J. Thompson, A comparison of the histopathology of premalignant and malignant mammary gland lesions induced in sexually immature rats with those occurring in the human. *Lab. Invest.* **80**, 221–231 (2000).

47. Y. Liu, Y. Zhao, J. Lyngsø, S. You, W. L. Wilson, H. Tu, S. A. Boppart, Suppressing short-term polarization noise and related spectral decoherence in all-normal dispersion fiber supercontinuum generation. *J. Lightwave Technol.* **33**, 1814–1820 (2015).

48. A. F. Pegoraro, A. Ridsdale, D. J. Moffatt, Y. Jia, J. P. Pezacki, A. Stolow, Optimally chirped multimodal CARS microscopy based on a single Ti:sapphire oscillator. *Opt. Express* **17**, 2984–2996 (2009).

49. V. V. Lozovoy, I. Pastirk, M. Dantus, Multiphoton intrapulse interference. IV. Ultrashort laser pulse spectral phase characterization and compensation. *Opt. Lett.* **29**, 775–777 (2004).